(Preprint) AAS XX-XXX

LINEAR COVARIANCE ANALYSIS FOR PROXIMITY OPERATIONS AROUND ASTEROID 2008 EV5

Cinnamon A. Wright[*], Sagar Bhatt[†], David Woffinden[‡], Matthew Strube[§], Chris D'Souza[¶]

The NASA initiative to collect an asteroid, the Asteroid Robotic Redirect Mission (ARRM), is currently investigating the option of retrieving a boulder from an asteroid, demonstrating planetary defense with an enhanced gravity tractor technique, and returning it to a lunar orbit. Techniques for accomplishing this are being investigated by the Satellite Servicing Capabilities Office (SSCO) at NASA GSFC in collaboration with JPL, NASA JSC, LaRC, and Draper Laboratory, Inc. Two critical phases of the mission are the descent to the boulder and the Enhanced Gravity Tractor demonstration. A linear covariance analysis is done for these phases to assess the feasibility of these concepts with the proposed design of the sensor and actuator suite of the Asteroid Redirect Vehicle (ARV). The sensor suite for this analysis includes a wide field of view camera, LiDAR, and an IMU. The proposed asteroid of interest is currently the C-type asteroid 2008 EV5, a carbonaceous chondrite that is of high interest to the scientific community. This paper presents an overview of the linear covariance analysis techniques and simulation tool, provides sensor and actuator models, and addresses the feasibility of descending to the surface of the asteroid within allocated requirements as well as the possibility of maintaining a halo orbit to demonstrate the Enhanced Gravity Tractor technique.

INTRODUCTION

The Asteroid Robotic Redirect Mission is evaluating two different options to fulfill the primary goal of redirecting a small asteroid or boulder and inserting it into a lunar orbit. Option A is to target and capture a ten-meter class asteroid (up to 1000 metric tons,) whereas Option B is to target a larger asteroid, collect a two- to four-meter boulder (up to 70 metric tons) from the surface, and perform a planetary defense demonstration.[1] Techniques for accomplishing this are being investigated by the Satellite Servicing Capabilities Office (SSCO) at NASA GSFC in collaboration with JPL, NASA JSC, LaRC, and Draper Laboratory, Inc. The planetary defense phase consists of an Enhanced Gravity Tractor (EGT) demonstration, which uses the gravitational force of the spacecraft and boulder to deflect the orbit of the asteroid. This concept was first proposed by Lu and Love in 2005.[2] A follow-on mission is being planned to then send astronauts to study the asteroid while it is in orbit around the moon. Previous work was done to develop a similar mission concept for Itokawa.[3] The focus of this paper will be to assess the feasibility of Option B given the current configuration for asteroid 2008 EV5.

Two critical phases of the mission are the descent to the surface of the asteroid and the planetary defense demonstration. A linear covariance analysis is performed for each of these phases. The next section gives a brief overview of linear covariance (LinCov) analysis and the tool utilized in this research. Then an overview

[*] Aerospace Engineer, Navigation and Mission Design Branch (Code 595), NASA Goddard Space Flight Center, Greenbelt MD, 20771, USA.
[†] Senior Member of Technical Staff, Charles Stark Draper Laboratory, Houston, TX 77058, USA.
[‡] Senior Member of Technical Staff, Charles Stark Draper Laboratory, Houston, TX 77058, USA.
[§] Aerospace Engineer, Components and Hardware Systems Branch (Code 596), NASA Goddard Space Flight Center, Greenbelt MD, 20771, USA.
[¶] GN&C Autonomous Flight Systems Engineer, NASA Johnson Spaceflight Center, 2101 NASA Parkway, Houston, TX, 77058, USA.

of the dynamics as well as the sensor and actuator models is presented. Finally the concept of operations, control logic, and results are discussed for each flight phase.

LINEAR COVARIANCE ANALYSIS OVERVIEW

In general, to perform the necessary analysis and evaluation of a GN&C system, there are several key variables of interest, including environment dispersions $\delta\mathbf{x}$, navigation dispersions $\delta\hat{\mathbf{x}}$, actual navigation error $\delta\mathbf{e}$, and onboard navigation error $\delta\hat{\mathbf{e}}$. These variables characterize the system's performance and are used to develop and validate mission objectives and requirements.[4] Extensive effort and resources are often allocated for the very purpose of producing and analyzing the quantities of these system parameters. For this paper, they are instrumental in characterizing the overall system and navigation performance for descending to the asteroid's surface and demonstrating the enhanced gravity tractor concept. This section is dedicated to formally defining these metrics and summarizing the analysis techniques and simulation tools adopted for obtaining them.

Performance Metric Definitions

The environment dispersions are defined as the difference between the environment state $\mathbf{x}$ and the nominal state $\bar{\mathbf{x}}$. The environment state is an $(n \times 1)$ vector that represents the true or actual state. The nominal state is also an $(n \times 1)$ vector that represents the desired or reference state. The covariance of the environment dispersions, $\mathbf{D}$, indicates how precisely the system can follow a desired trajectory.

$$\delta\mathbf{x} \triangleq \mathbf{x} - \bar{\mathbf{x}}, \qquad \mathbf{D} = E\left[\delta\mathbf{x}\delta\mathbf{x}^{\mathrm{T}}\right] \tag{1}$$

The environment (or true) dispersions are often referred to as simply *dispersions* (e.g., trajectory dispersions, position dispersions, relative dispersions).

The navigation dispersions are defined as the difference between the navigation state $\hat{\mathbf{x}}$ and the nominal state. The navigation state is an $(\hat{n} \times 1)$ vector that represents the estimated state.

$$\delta\hat{\mathbf{x}} \triangleq \hat{\mathbf{x}} - \mathbf{N}\bar{\mathbf{x}}, \qquad \hat{\mathbf{D}} = E\left[\delta\hat{\mathbf{x}}\delta\hat{\mathbf{x}}^{\mathrm{T}}\right] \tag{2}$$

The matrix $\mathbf{N}$ is an $(\hat{n} \times n)$ mapping matrix that defines the estimated state in terms of the true and nominal state. It typically *cancels* the attitude rate state when gyro measurements are incorporated in lieu of an angular rate estimate. An inverse mapping takes the estimated state to the true state, represented with an $(n \times \hat{n})$ matrix $\mathbf{N}^{\mathrm{T}}$. The covariance of the navigation dispersions, $\hat{\mathbf{D}}$, reflect how precisely the onboard system thinks it can follow a prescribed reference trajectory.

The true navigation error is the difference between the environment and navigation states. It is also the difference between the environment and the navigation dispersions.

$$\delta\mathbf{e} \triangleq \mathbf{N}\mathbf{x} - \hat{\mathbf{x}} = \mathbf{N}\delta\mathbf{x} - \delta\hat{\mathbf{x}}, \qquad \mathbf{P} = E\left[\delta\mathbf{e}\delta\mathbf{e}^{\mathrm{T}}\right] \tag{3}$$

The covariance of the true navigation error, $\mathbf{P}$, characterizes how precisely the onboard navigation system can determine the actual state. The onboard navigation error is never computed but is used to develop the onboard navigation filter equations. It is defined as the difference between the design state, x, and the navigation state.

$$\delta\hat{\mathbf{e}} \triangleq \mathrm{x} - \hat{\mathbf{x}}, \qquad \hat{\mathbf{P}} = E\left[\delta\hat{\mathbf{e}}\delta\hat{\mathbf{e}}^{\mathrm{T}}\right] \tag{4}$$

The covariance of the onboard navigation error, $\hat{\mathbf{P}}$, shows how precisely the onboard navigation system thinks it can determine the actual state. The performance of the onboard navigation system is determined by comparing $\hat{\mathbf{P}}$ to the actual navigation performance $\mathbf{P}$. It is the covariances of the true dispersions, navigation dispersions, true navigation error, and the onboard navigation error that are ultimately used to analyze and assess the performance of a proposed GN&C system.

Obtaining the Performance Metrics

A common approach to obtain these performance metrics is to use a Monte Carlo simulation as shown in Figure 1, where the sample statistics of hundreds or thousands of runs are used to numerically compute the desired covariance matrices.

$$\mathbf{D} = \frac{1}{N-1}\sum \delta\mathbf{x}\delta\mathbf{x}^{\mathrm{T}} \qquad \hat{\mathbf{D}} = \frac{1}{N-1}\sum \delta\hat{\mathbf{x}}\delta\hat{\mathbf{x}}^{\mathrm{T}}$$
$$\mathbf{P} = \frac{1}{N-1}\sum \delta\mathbf{e}\delta\mathbf{e}^{\mathrm{T}}$$

This same statistical information can be obtained using linear covariance analysis techniques[5,6,7,8] by directly propagating, updating, and correcting an augmented state covariance matrix $\mathbf{C}$,

$$\mathbf{C} = E\left[\delta\mathbf{X}\delta\mathbf{X}^{\mathrm{T}}\right] \tag{5}$$

where the augmented state $\delta\mathbf{X}^{\mathrm{T}} = [\delta\mathbf{x}^{\mathrm{T}}\ \delta\hat{\mathbf{x}}^{\mathrm{T}}]$ consists of the true dispersions and the navigation dispersions. Notice that by simply pre- and post-multiplying the augmented state covariance matrix by the following matrices, the covariance matrices for the trajectory dispersions, navigation dispersions, and the navigation error can be obtained.

$$\mathbf{D} = \left[\ \mathbf{I}_{n\times n},\ \mathbf{0}_{n\times n}\mathbf{N}^{\mathrm{T}}\ \right]\mathbf{C}\left[\ \mathbf{I}_{n\times n},\ \mathbf{0}_{n\times n}\mathbf{N}^{\mathrm{T}}\ \right]^{\mathrm{T}} \qquad \hat{\mathbf{D}} = \left[\ \mathbf{N0}_{n\times n},\ \mathbf{I}_{\hat{n}\times\hat{n}}\ \right]\mathbf{C}\left[\ \mathbf{N0}_{n\times n},\ \mathbf{I}_{\hat{n}\times\hat{n}}\ \right]^{\mathrm{T}}$$
$$\mathbf{P} = \left[\ \mathbf{NI}_{n\times n},\ -\mathbf{I}_{\hat{n}\times\hat{n}}\ \right]\mathbf{C}\left[\ \mathbf{NI}_{n\times n},\ -\mathbf{I}_{\hat{n}\times\hat{n}}\ \right]^{\mathrm{T}}$$

Consequently, Monte Carlo and linear covariance analysis techniques provide a complimentary analysis package since they each generate the same statistical information using different approaches. The strengths and weaknesses of one technique often offset the other. Such is the case when developing and analyzing the preliminary trajectory design and concept of operations for close-proximity asteroid operations.

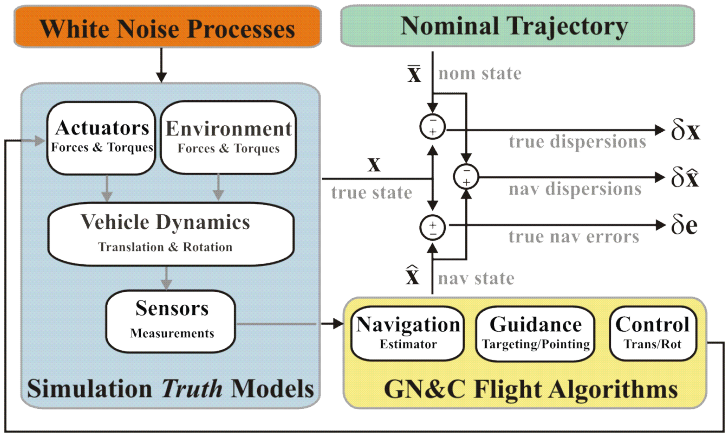

Figure 1. GN&C Performance Metrics in a Generic Monte Carlo Simulation[4]

SIMULATION OVERVIEW

For this preliminary design phase and feasibility study, a linear covariance analysis tool is utilized. Minor adjustments are made to a previously developed rendezvous and docking LinCov simulation[8,9] by including the gravitational attraction between both the target (asteroid) and chaser (ARV) bodies, which is typically neglected in rendezvous scenarios between two orbiting vehicles. For this simulation, the absolute states of the ARV and the target asteroid are modeled in the Sun-Centered Inertial reference frame. The asteroid 2008

EV5 is considered in this paper. It has a mass of m_t=1.05E+11 kg,[10] a gravitational parameter of 7 m^3/s, and a radius of 200 m. The asteroid trajectory and initial position and velocity is obtained from a Horizons .bsp file.[11] The initial attitude is $\mathbf{q_t}$ = [-0.1812, -0.9587, 0.1929, 0.1039], and the asteroid rotates about its north pole with a four hour period. The asteroid inertia, $\mathbf{J_t}$, has moments of inertia [4.42855, 4.48630, 4.76455] 10^{15} kg·m^2 computed using dimensions from Reference 10 and zero products of inertia.

The ARV mass is m_c=9000 kg, and ARV inertia, $\mathbf{J_c}$, has moments of inertia [81886.5, 120382.5, 117450] kg·m^2 and zero products of inertia. The simulation starts on December 31, 2023, and uses a fourth-order Runge-Kutta method with a 1 s time step. A spherical gravity field and J2000 reference frame centered at the Sun are utilized.The relative initial state in Asteroid-Centered Inertial reference frame is a position of [-152.85 -158.54 333.91] m and a velocity of [-7.161 85.66 37.397] mm/s with and initial attitude of $\mathbf{q_c}$ =[0.1988, -0.0032, -0.9578, -0.2076]. The relative states are estimated using a suite of sensors described later in this section. The relative 3σ uncertainty in the initial states is as follows: 10 m in position, 5 mm/s in velocity, 1 deg in attitude, 1 arcsec/s in attitude rate. The 3σ process noise is 1.1727E-6 m/s/$\sqrt{\text{s}}$ for translation and 0.001E-9 rad/$\sqrt{\text{s}}$ for rotation. The translational and rotational maneuver execution errors are given in Tables 4 and 5. The concept of operations for each phase will be discussed in more detail later.

Dynamic Modeling

The asteroid rendezvous simulation models include the chaser and target translation and rotational dynamics; disturbance accelerations and torques; strap-down inertial measurement units (IMUs), optical navigation camera, and FPOSE (from Flash LiDAR pose) measurements; and the torques and velocity changes generated by momentum wheels and thrusters. The truth model state is defined by 13 target states $\mathbf{x}_t$, 13 chaser states $\mathbf{x}_c$, and parameter states associated with various aspects of the sensors used onboard the chaser $\mathbf{x}_p$. The 13 asteroid target states include the inertial position and velocity vectors, the quaternion defining the orientation of the target with respect to the inertial frame, and the target's angular rate coordinatized in the target reference frame. Similarly, the 13 chaser states are inertial position and velocity, the inertial-to-body quaternion, and angular rate. The k parameter states such as the sensor or actuator biases, misalignments, scale factor terms, and other error sources are modeled as first-order Markov processes with time constants, τ_k.

$$\mathbf{x} = \left[\mathbf{x}_t;\ \mathbf{x}_c;\ \mathbf{x}_p\right]^T \tag{6}$$

$$\mathbf{x}_t = \left[\mathbf{r}_t;\ \mathbf{v}_t;\ \mathbf{q}_i^t;\ \boldsymbol{\omega}_t^t\right]^T \qquad \mathbf{x}_c = \left[\mathbf{r}_c;\ \mathbf{v}_c;\ \mathbf{q}_i^c;\ \boldsymbol{\omega}_c^c\right]^T \qquad \mathbf{x}_p = \left[\mathbf{x}_{p1};\ \mathbf{x}_{p2};\ ...;\ \mathbf{x}_{pk}\right]^T \tag{7}$$

The dynamics for the chaser, target, and parameter states are defined as,

$$\dot{\mathbf{r}}_t = \mathbf{v}_t \tag{8}$$

$$\dot{\mathbf{v}}_t = \mathbf{g}_t + \boldsymbol{\eta}_{a_t} \tag{9}$$

$$\dot{\bar{\mathbf{q}}}_i^t = \frac{1}{2}\,\boldsymbol{\omega}_t^t \otimes \bar{\mathbf{q}}_i^t \tag{10}$$

$$\dot{\boldsymbol{\omega}}_t^t = \mathbf{J}_t^{-1}\left[\boldsymbol{\tau}_g^t - \boldsymbol{\omega}_t^t \times \mathbf{J}_t\boldsymbol{\omega}_t^t\right] + \boldsymbol{\eta}_{\alpha_t} \tag{11}$$

$$\dot{\mathbf{r}}_c = \mathbf{v}_c \tag{12}$$

$$\dot{\mathbf{v}}_c = \mathbf{g}_c + \mathbf{a}_{ctrl} + \boldsymbol{\eta}_{a_c} \tag{13}$$

$$\dot{\bar{\mathbf{q}}}_i^c = \frac{1}{2}\,\boldsymbol{\omega}_c^c \otimes \bar{\mathbf{q}}_i^c \tag{14}$$

$$\dot{\boldsymbol{\omega}}_c^c = \mathbf{J}_c^{-1}\left[\boldsymbol{\tau}_{ctrl}^c + \boldsymbol{\tau}_g^c - \boldsymbol{\omega}_c^c \times \mathbf{J}_c\boldsymbol{\omega}_c^c\right] + \boldsymbol{\eta}_{\alpha_c} \tag{15}$$

$$\dot{\mathbf{x}}_{pk} = -\mathbf{x}_{pk}/\tau_k + \boldsymbol{\eta}_{pk} \tag{16}$$

where $\mathbf{J}_t$ and $\mathbf{J}_c$ are the target and chaser inertia matrices, respectively. The accelerations due to gravity acting on the target and chaser vehicles, $\mathbf{g}_t$ and $\mathbf{g}_c$, are based on multi-body point-mass gravity terms. The gravitational torques, $\boldsymbol{\tau}_g^t$ and $\boldsymbol{\tau}_g^c$, are derived from Wertz.[12] The control inputs, $\mathbf{a}_{ctrl}$ and $\boldsymbol{\tau}_{ctrl}^c$, are the accelerations and torques executed by the actuators on the chaser spacecraft defined in Eq. (27) and Eq. (29) respectively. The random disturbances, $\boldsymbol{\eta}_{a_t}$, $\boldsymbol{\eta}_{\alpha_t}$, $\boldsymbol{\eta}_{a_c}$, and $\boldsymbol{\eta}_{\alpha_c}$, are included in the models to account for unmodeled forces and torques acting on each body such as drag, solar radiation pressure, venting gases, etc.

Sensor Modeling

The analysis assumes several different sensors, including an optical camera, FPOSE, and an IMU. The mounting configurations of the cameras are illustrated in Figure 2.

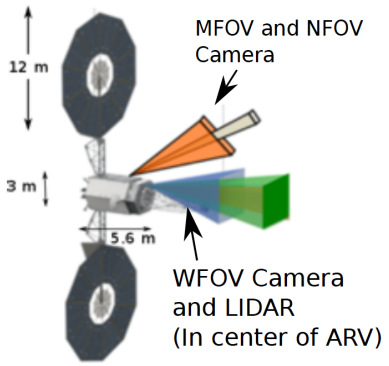

Figure 2. ARV and Sensor Locations

Measurement Frequency	10	s
Distortion Coefficient	[0.06 0 0]	
Resolution	2592 x 1944	
Focal Length	4.7	mm
Medium Field of View (MFOV)	10	deg
Wide Field of View (WFOV)	30	deg
Measurement Noise	1	pixels
Pixel Density	2758	pixels/mm

Table 1. Camera Parameters

Optical Camera Model The optical camera model is based on the models described in the references by Owen[13] and D'Souza.[14] The parameters for the cameras currently baselined for the mission and used in this simulation are given in Table 1. A process called Stereophotoclinometry (SPC)[15] will be used for the optical navigation. This process includes generating maplets and correlating images, and landmarks within images, with those maplets. Landmark locations are identified as columns of the matrix $\mathbf{l}^t_{lmrk}$. The landmark positions are specified in the target body frame and transformed to the inertial frame as $\mathbf{l}^i_{lmrk} = \mathbf{T}^i_t \mathbf{l}^t_{lmrk}$. The location of the landmark in the inertial frame is the position of the asteroid plus the landmark position relative to the center of the asteroid $\mathbf{r}^i_{lmrk} = \mathbf{r}^i_t + \mathbf{l}^i_{lmrk}$. Assuming the camera is at the center-of-mass of the chaser vehicle, if the chaser position is known in the inertial frame $\mathbf{r}^i_c$ then the apparent vector in the inertial frame is simply the difference $\mathbf{a}^i_{lmrk} = \mathbf{r}^i_{lmrk} - \mathbf{r}^i_c$, as depicted in Figure 3(b).

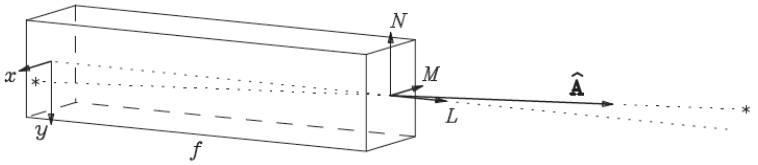

(a) Camera and coordinate systems[13]

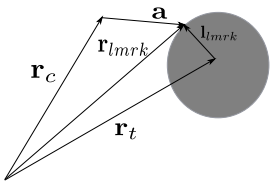

(b) Apparent position of landmark, $\mathbf{a}$, position of camera $\mathbf{r}_c$, position of asteroid $\mathbf{r}_t$, and position of landmark with respect to the asteroid $\mathbf{l}_{lmrk}$

Figure 3. Optical Navigation Model Definitions

The apparent location of the landmark feature relative to the camera in the optical camera frame, $\mathbf{a}^o_{lmrk}$, as shown in Figure 3(a) is

$$\mathbf{a}^o_{lmrk} = \mathbf{A} = [M\ N\ L] = \mathbf{T}^o_i \mathbf{a}^i_{lmrk} \tag{17}$$

where $\mathbf{T}^o_i$ is the rotation matrix from the inertial frame to the optical camera frame. Expanding Eq. (17), the apparent location of the landmark features can be expressed in terms of the navigation states, which include the target inertial position $\mathbf{r}^i_t$, the target orientation uncertainty $\boldsymbol{\theta}^t_i$, the chaser inertial position $\mathbf{r}^i_c$, and the chaser attitude error $\boldsymbol{\theta}^c_c$.

$$\mathbf{a}^o_{lmrk} = \mathbf{T}^o_c(\mathbf{I} - [\boldsymbol{\theta}^c_c\times])\hat{\mathbf{T}}^c_i \left[\mathbf{r}^i_t + \hat{\mathbf{T}}^i_t(\mathbf{I} + [\boldsymbol{\theta}^t_t\times])\mathbf{l}^t_{lmrk} - \mathbf{r}^i_c\right] \tag{18}$$

At the detector, the image appears inverted with pixel coordinates (x,y) which are a function of the apparent location of the landmarks $A = \mathbf{a}^o_{lmrk}$, the camera focal length f, and the pixel biases, b_x and b_y.

$$\begin{pmatrix} x \\ y \end{pmatrix} = \frac{f}{A_L} \begin{pmatrix} A_M \\ A_N \end{pmatrix} + \begin{pmatrix} b_x \\ b_y \end{pmatrix} \tag{19}$$

The logic to determine whether the landmark is visible is then executed. Radial distortion is added which distorts the image toward or away from the optical axis. Tip and tilt terms are added to account for misalignment due to the detector not being perfectly perpendicular to the optical axis. Then the corrected image locations

$$\begin{pmatrix} x^{'} \\ y^{'} \end{pmatrix} = \begin{pmatrix} x \\ y \end{pmatrix} + \begin{pmatrix} xr^2 & xy & x^2 \\ yr^2 & y^2 & xy \end{pmatrix} \begin{pmatrix} \epsilon_1 \\ \epsilon_2 \\ \epsilon_3 \end{pmatrix} \tag{20}$$

are transformed to pixel, s and l line coordinates,

$$\begin{pmatrix} s \\ l \end{pmatrix} = \begin{pmatrix} K_x & K_{xy} \\ K_{yx} & K_y \end{pmatrix} \begin{pmatrix} x^{'} \\ y^{'} \end{pmatrix} + \begin{pmatrix} s_o \\ l_o \end{pmatrix} \tag{21}$$

where $\mathbf{K}$ contains the reciprocal of the pixel dimensions.[13] Additional logic has been implemented to check whether each landmark is within the FOV of the camera and to enforce a minimum maplet resolution of 10 cm.

FPOSE Model FPOSE uses LiDAR data to generate a six degree-of-freedom position and orientation measurement relative to a target object. This will be used for the descent phase and the target will be the boulder of interest. The measurement is modeled with a constant and a Markov bias.[16] The relative position vector in the FPOSE frame is given by the equation

$$\tilde{\mathbf{r}}^f_{rel} = \mathbf{T}^f_b \mathbf{T}^b_i (\mathbf{r}_t - \mathbf{r}_c) + \mathbf{b}^f_\rho + \boldsymbol{\beta}^f_\rho + \boldsymbol{\eta}^f_\rho \ , \tag{22}$$

where $\mathbf{r}_t$ and $\mathbf{r}_c$ are the target and chaser inertial position vectors, $\mathbf{b}^f_\rho$ is the relative position constant bias, $\boldsymbol{\beta}^f_\rho$ is the relative position Markov bias, and $\boldsymbol{\eta}^f_\rho$ is the relative position measurement noise.

The relative attitude measurement in the FPOSE sensor frame is processed as a derived measurement, $\tilde{\boldsymbol{\theta}}^f_{rel}$. It is effectively the residual to be processed by the onboard navigation filter,

$$\boldsymbol{I} - \left[\tilde{\boldsymbol{\theta}}^f_{rel}\times\right] = \tilde{\mathbf{T}}^f_t \left[\hat{\mathbf{T}}^t_i \hat{\mathbf{T}}^i_c \hat{\mathbf{T}}^c_f\right] \tag{23}$$

where the estimate of the derived relative attitude measurement is a function of the target attitude uncertainty $\boldsymbol{\theta}^t_t$, the chaser attitude error state $\boldsymbol{\theta}^c_c$, the constant bias $\mathbf{b}^f_\theta$, a Markov bias $\boldsymbol{\beta}^f_\theta$, and noise $\boldsymbol{\eta}^f_\theta$.

$$\tilde{\boldsymbol{\theta}}^f_{rel} = \hat{\mathbf{T}}^f_t \boldsymbol{\theta}^t_t - \hat{\mathbf{T}}^f_c \boldsymbol{\theta}^c_c + \mathbf{b}^f_\theta + \boldsymbol{\beta}^f_\theta + \boldsymbol{\eta}^f_\theta \tag{24}$$

The Markov and constant bias 3σ uncertainties for translation and orientation were 57 cm and 1 deg with a time constant of 600 s and 19 cm and 1 degree of measurement noise. The FPOSE uncertainty parameters used for this simulation were obtained from test data with a satellite mock-up as the target. A test campaign to collect data that more closely represents this scenario is planned for the future.

IMU Model The gyro model is based upon a package of three orthogonal strapdown gyros, each measuring the chaser's angular velocity along its input axis. The measured angular velocity is a function of the true angular rate $\boldsymbol{\omega}^c$ with a gyro bias $\boldsymbol{\beta}^{imu}_g$, scale factor $\mathbf{s}^{imu}_g$, misalignment $\boldsymbol{\mu}^{imu}_g$, and the gyro angular random walk $\boldsymbol{\upsilon}^{imu}_g$.

$$\tilde{\boldsymbol{\omega}}^{imu} = \mathbf{T}\left(\boldsymbol{\mu}^{imu}_g\right)\left\{\mathbf{I} + \left[\mathbf{s}^{imu}_g \backslash\right]\right\} \mathbf{T}^{imu}_c \boldsymbol{\omega}^c + \boldsymbol{\beta}^{imu}_g + \boldsymbol{\upsilon}^{imu}_g \tag{25}$$

The gyro performance parameters are summarized in Table 2.

The measured accelerations from the accelerometers are a function of the non-gravitational accelerations $\mathbf{a}^i$, the accelerometer bias $\boldsymbol{\beta}^{imu}_a$, scale factor $\mathbf{s}^{imu}_a$, misalignment $\boldsymbol{\mu}^{imu}_a$, and the accelerometer random walk $\boldsymbol{\upsilon}^{imu}_a$.

$$\tilde{\mathbf{a}}^{imu} = \mathbf{T}\left(\boldsymbol{\mu}^{imu}_a\right)\left\{\mathbf{I} + \left[\mathbf{s}^{imu}_a \backslash\right]\right\} \mathbf{T}^{imu}_c \, \mathbf{T}^c_i \, \mathbf{a}^i + \boldsymbol{\beta}^{imu}_a + \boldsymbol{\upsilon}^{imu}_a \tag{26}$$

The accelerometer performance parameters are summarized in Table 3.

Constant Bias		
Angle Random Walk Uncertainty	0.018	deg/$\sqrt{\text{hr}}$ (3σ)
Bias Uncertainty	0.45	deg/hr (3σ)
Scale Factor Uncertainty	15	ppm (3σ)
Misalignment Uncertainty	75	arcsec (3σ)
Markov Bias		
Time Constant	100	s
SS Uncertainty	0.09	deg/hr (3σ)
Markov Scale Factor		
Time Constant	100	s
SS Uncertainty	100	ppm (3σ)

Table 2. Gyro Parameters

Constant Bias		
Velocity Random Walk Uncertainty	150	μg/$\sqrt{\text{Hz}}$ (3σ)
Bias Uncertainty	300	μg (3σ)
Scale Factor Uncertainty	525	ppm (3σ)
Misalignment Uncertainty	45	arcsec (3σ)
Markov Bias		
Time Constant	60	s
SS Uncertainty	45	μg (3σ)
Markov Scale Factor		
Time Constant	100	s
SS Uncertainty	525	ppm (3σ)

Table 3. Accelerometer Parameters

Actuators

Actuators are used to manipulate the spacecraft's translational and rotational velocities. The actual acceleration $\mathbf{a}^i_{ctrl}$ is a function of the commanded acceleration $\hat{\mathbf{a}}^i_{cmd}$ plus an associated maneuver bias $\mathbf{b}_{mvr}$, scale factor $\mathbf{s}_{mvr}$, misalignment $\boldsymbol{\mu}_{mvr}$, and execution noise $\boldsymbol{\eta}_{mvr}$ terms.

$$\mathbf{a}^i_{ctrl} = \mathbf{T}^i_c \mathbf{T}\left(\boldsymbol{\mu}_{mvr}\right)\left[\left\{\mathbf{I} + [\mathbf{s}_{mvr}\backslash]\right\}\hat{\mathbf{T}}^c_i \hat{\mathbf{a}}^i_{cmd} + \mathbf{b}_{mvr} + \boldsymbol{\eta}_{mvr}\right] \tag{27}$$

The commanded acceleration is computed using a proportional-derivative (PD) controller

$$\hat{\mathbf{a}}^i_{cmd} = \boldsymbol{K}_r\left(\bar{\mathbf{r}} - \hat{\mathbf{r}}\right) + \boldsymbol{K}_v\left(\bar{\mathbf{v}} - \hat{\mathbf{v}}\right) \tag{28}$$

The reaction control system (RCS) produces the torques required to alter the chaser's attitude rate. The imparted torque is modeled as a function of the commanded torque $\hat{\boldsymbol{\tau}}^c_{cmd}$ plus a torque bias $\mathbf{b}_{rot}$, scale factor $\mathbf{s}_{rot}$, misalignment $\boldsymbol{\mu}_{rot}$, and noise $\boldsymbol{\eta}_{rot}$ terms.

$$\boldsymbol{\tau}^c_{ctrl} = \mathbf{T}\left(\boldsymbol{\mu}_{rot}\right)\left[\left\{\mathbf{I} + [\mathbf{s}_{rot}\backslash]\right\}\hat{\boldsymbol{\tau}}^c_{cmd} + \mathbf{b}_{rot} + \boldsymbol{\eta}_{rot}\right] \tag{29}$$

The commanded torques are also computed using a PD controller to achieve the desired orientation

$$\hat{\boldsymbol{\tau}}^c_{cmd} = \mathbf{J_c}\left\{\boldsymbol{K}_\theta\left(\delta\boldsymbol{\theta}^c\right) + \boldsymbol{K}_\omega\left(\bar{\boldsymbol{\omega}}^c_c - \hat{\boldsymbol{\omega}}^c_c\right)\right\} \tag{30}$$

where $\delta\boldsymbol{\theta}^c$ is the 3-element rotation vector representing the angular difference between the desired attitude quaternion $\bar{\mathbf{q}}^i_c$ and the actual attitude $\mathbf{q}^i_c$. The translational and rotational gains in this paper are $\boldsymbol{K}_r = \boldsymbol{K}_\theta = \omega_n^2$ and $\boldsymbol{K}_v = \boldsymbol{K}_\omega = 2\zeta\omega_n$, with natural frequency $\omega_n = 2\pi/600$ rad/s and damping ratio $\zeta = \sqrt{2}/2$. The translational and rotational maneuver execution errors are summarized in Tables 4 and 5 respectively.

DESCENT TO THE ASTEROID SURFACE

One of the most critical phases of the mission is the descent to the surface of the asteroid. To successfully collect the boulder, the capture arms must be centered directly over the object to within 50 cm. The descent phase starts 50 m above the surface of the asteroid. The spin rate of the spacecraft is controlled to stay above the boulder. Six degree-of-freedom control is applied until the ARV is 20 m above the surface. From that point on, control is only applied in the horizontal direction and the gravitational force of the asteroid is allowed to pull the ARV to the surface. At 20 m, the downward velocity is required to be 7 cm/s or less. Measurements are processed for seven different landmarks which are shown with the trajectory in Figure 4(a). One landmark is located at the top of the boulder and the other landmarks are 10 and 25 meters away in different directions. In this scenario, it takes about 15 minutes to descend from 50 meters above the surface to the surface of the asteroid.

Bias Initial Uncertainty	1	mN
Scale Factor Initial Uncertainty	1000	ppm
Misalignment Initial Uncertainty	1	mrad
Bias Time Constant	10000	sec
Scale Time Constant	10000	sec
Misalignment Time Constant	10000	sec
Process Noise	150	mN/$\sqrt{s}$

Table 4. Translational 3σ Maneuver Errors

Bias Initial Uncertainty	1	mN·mm
Scale Factor Initial Uncertainty	100	ppm
Misalignment Initial Uncertainty	1	mrad
Bias Time Constant	10000	sec
Scale Time Constant	10000	sec
Misalignment Time Constant	10000	sec
Process Noise	3e-7	mNm/$\sqrt{s}$

Table 5. Rotational 3σ Maneuver Errors

Control Logic

The translational and rotational control logic each implement PD controllers as described in Eq. (28) and Eq. (30) respectively. The attitude guidance is designed to align the boulder capture mechanism (along the ARV axis of symmetry) with the desired line of descent, which is fixed in the asteroid frame. The desired angular rate is about the direction of translational acceleration. The translational guidance relies upon a pre-planned reference trajectory (relative position and velocity), delivered by the rendezvous and proximity operations team at GSFC until the ARV reaches 20 m above the surface. At this point the control logic inhibits thruster firings along the direction normal to the asteroid surface to avoid pluming the boulder, letting the asteroid's gravity pull the ARV to the surface.

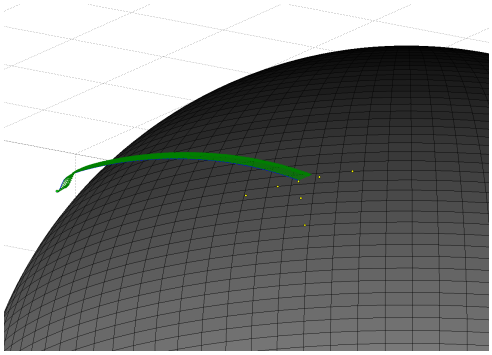

(a) Nominal Descent Trajectory with Landmarks

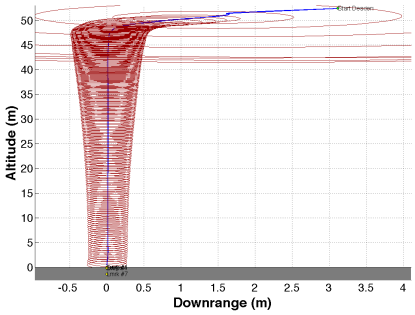

(b) Dispersions Along Nominal Trajectory

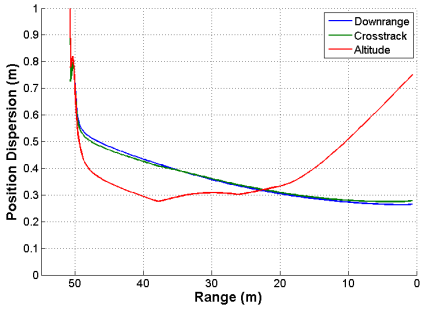

(c) Relative 3σ Position Environment Dispersions

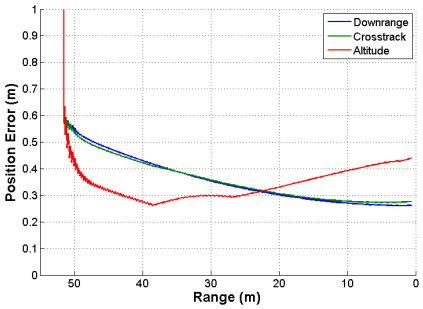

(d) Relative 3σ Position Navigation Errors

Figure 4. Dispersion and Navigation Errors for Descent Phase

Results

A requirement for the boulder capture phase is for the horizontal dispersions to remain within 50 cm. Figures 4(b) - 4(d) show the dispersions and navigation errors for this scenario. The dispersions in the altitude direction increase drastically after 20 m because no control is applied in that direction but the crosstrack and downrange dispersions are well within the requirement, at about 25 cm.

ENHANCED GRAVITY TRACTOR DEMONSTRATION

A secondary goal of this mission is to demonstrate planetary defense capabilities. The effect of deflecting an asteroid kinematically can be uncertain, especially since many asteroids are rubble piles. The path of an asteroid can be deflected by hovering, or in this case maintaining a halo orbit, in front of the asteroid. This technique uses the gravitational force of the boulder and the spacecraft to deflect the asteroid.[17] After collecting the boulder, the spacecraft will maneuver to a safe distance away from the asteroid and perform analyses to better estimate the new mass properties of the spacecraft and boulder. The spacecraft will then insert into a halo orbit around the velocity direction of the asteroid, r = 1 km from the center of the asteroid, and remain there for six days. The spacecraft will then transition to a halo orbit r = 400 m from the center of the asteroid (with a halo orbit radius of $r_h = 346m$) and remain there for 30 days. At this point, the Wide FOV Camera and the LiDAR will be blocked by the boulder, so only the Medium and Narrow FOV cameras will be available. At this distance the MFOV sensor will be most useful. Because of the location of the camera, shown in Figure 2, the camera will only be pointed toward the asteroid during half of the orbit, unless the ARV rotates to point the camera in the other direction. The halo orbit is shown in Figure 5(a).

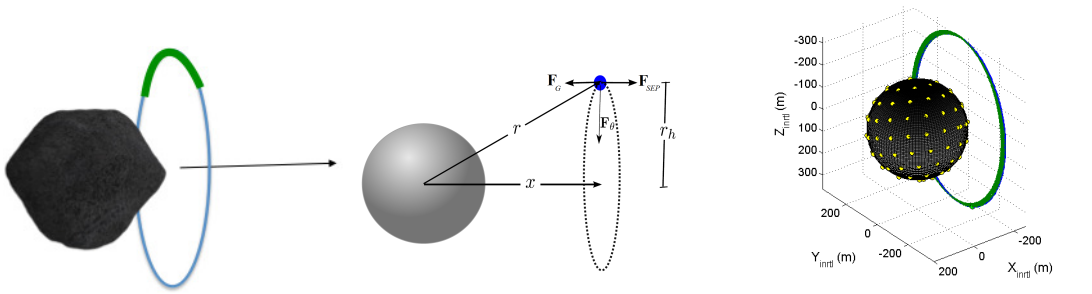

(a) Gravity Tractor Halo Orbit (b) Dispaced Orbit Gravity Tractor (c) Nominal Trajectory in Inertial Frame

Figure 5. Gravity Tractor Halo Orbit

Control Logic

One option that was investigated for the EGT demonstration was to use only the Solar Electric Propulsion (SEP) System to supply a constant force to counteract the component of gravitational force along the asteroid's velocity vector[17] as shown in Figure 5(b)

$$F_{SEP} = -F_G = \frac{Gm_t(m_c + m_b)}{r^2}\left(\frac{x}{r}\right) \tag{31}$$

where m_t, m_c, and m_b are the mass of the asteroid, spacecraft, and boulder respectively. The initial velocity for the halo orbit is set so that the centripetal acceleration of the halo orbit equals the vertical component of the gravitational force due to the asteroid $v_z = r_h\omega$, where r_h is the radius of the halo orbit. The radius of the halo orbit is also set so that the thrusters do not plume the surface of the asteroid. Another option is to use a PD controller to maintain a desired halo orbit. The performance results of both techniques are investigated.

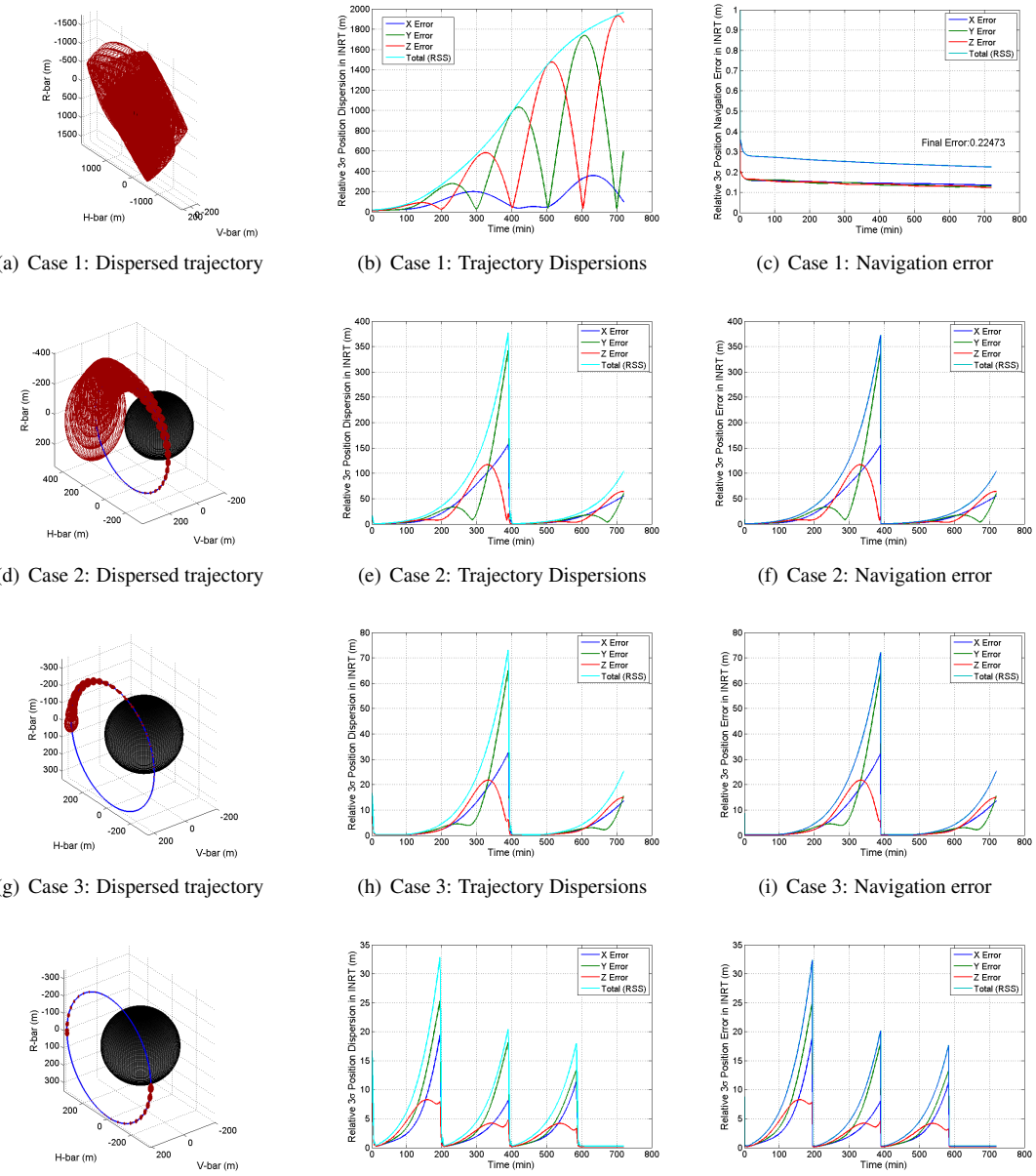

(a) Case 1: Dispersed trajectory (b) Case 1: Trajectory Dispersions (c) Case 1: Navigation error

(d) Case 2: Dispersed trajectory (e) Case 2: Trajectory Dispersions (f) Case 2: Navigation error

(g) Case 3: Dispersed trajectory (h) Case 3: Trajectory Dispersions (i) Case 3: Navigation error

(j) Case 4: Dispersed trajectory (k) Case 4: Trajectory Dispersions (l) Case 4: Navigation error

Figure 6. Halo orbit performance results.

Results

Several factors such as halo orbit size, orbit maintenance strategy, unmodeled accelerations, measurement pass duration, frequency of each available measurement pass, camera field-of-view, number of features tracked, and resolution influence the overall gravity tractor performance. Although each of these have been investigated, this paper will focus on several that influenced the overall vehicle and mission operations, including orbit maintenance strategy, measurement pass duration, and measurement pass frequency.

The nominal trajectory provided in Figure 5(c) is used to investigate the closed-loop GN&C performance with four different test cases: 1) constant thrust profile with continuous measurements, 2) closed-loop PD

controller with a 10 minute measurement pass duration once per orbit, 3) closed-loop PD controller with a 90 minute measurement pass once per orbit, and 4) closed-loop PD controller with a 10 minute measurement pass twice per orbit. For these cases, a generic relative sensor is used to highlight important trends, but the camera model has also been incorporated to confirm performance levels and show the expected measurement pass duration as a function of field-of-view and the number of features.

Figures 6(a) - 6(c) show the results for Case 1 in which continuous thrust is applied while processing continuous measurements. Due to the instability of the gravity tractor orbit, even though the navigation error stays tightly bounded and constant thrust is applied, the dispersions grow to almost 2 km. This highlights the limitations of using a simple constant thrust halo orbit strategy and emphasizes the need for a feedback control implementation for long duration halo orbit maintenance.

Figures 6(d) - 6(f) show the results for Case 2 which illustrates the advantage of using a closed-loop PD controller for maintaining the vehicle on the halo orbit. Although the nominal thrust profiles for the PD controller and the constant thrust methodologies are largely the same, the resulting trajectory dispersions are drastically reduced from several kilometers to several hundred meters by incorporating a feedback controller. For this second scenario, the measurement pass duration was limited to 10 minutes and only one measurement pass was allocated per orbit.

Figures 6(g) - 6(i) show the results for Case 3 where a PD controller is used but the measurement pass duration is extended from 10 minutes to 90 minutes. This represents the scenario where either the camera FOV is increased or the camera is gimbaled to track landmark features for longer periods. By tracking the features for a longer duration, the maximum 3σ RSS trajectory dispersion dropped from 370 m to 70 m. The improvement comes because the time required to propagate the navigation solution in between measurement passes is reduced. Since the trajectory dispersions largely follow the navigation error when using a PD controller, the trajectory dispersions are reduced by limiting the error growth due to propagating the navigation solution.

Figures 6(j) - 6(l) show the results for Case 4 which uses a PD controller and only a 10 minute measurement pass duration but with the frequency of measurement passes increased from once per orbit to twice per orbital period. Although not formally derived at this phase, it is desired that the maximum 3σ RSS trajectory dispersions remain within 50 m. This accuracy can be accomplished by having short but more frequent measurement passes. So even though the measurement duration is only 10 minutes, the maximum 3σ RSS relative trajectory dispersions are less than 35 m when the frequency is twice per orbit.

Figure 7 provides a breakdown of the major factors such as initial condition uncertainty, maneuver execution errors, process noise (unmodeled accelerations), sensor accuracy, and other environment disturbances that contribute to the overall relative position dispersions. This error budget[4] is generated using Case 4 as an example because this scenario represents the recommended approach where potentially short measurement passes occur multiple times per orbit. In Figure 7, the solid dark (maroon) line represents the 3σ RSS relative position dispersions given all the potential error sources as previously shown in Figure 6(k). The contribution of each error source is then represented with a corresponding line and their RSS value is shown with the dashed light (cyan) colored line. These results show the long-term dominating error sources are sensor measurement and maneuver execution errors.

CONCLUSIONS

These results demonstrate that with the current set of sensors baselined for the ARRM Option B mission it is feasible to meet requirements for the boulder capture phase of the mission. Using only a continuous, open-loop, thrust profile to maintain the gravity tractor halo orbit, however, is not feasible when accounting for unknown perturbations. The instability of the halo orbit requires a closed-loop controller for long term orbit maintenance and it is recommended that a second measurement arc be added to decrease the navigation error. Future analyses are planned to model thruster locations, throttling, and gimbaling.

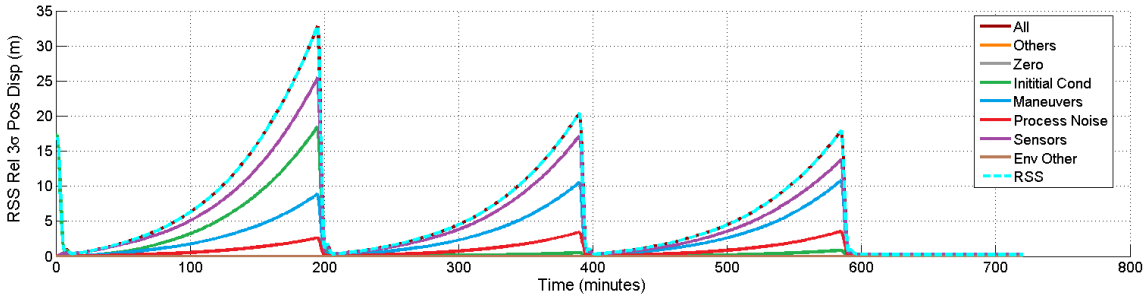

Figure 7. Relative 3σ Trajectory Dispersion Error Budget (Case 4)

ACKNOWLEDGMENT

The authors would like to give a special thank you to David Reeves and Bo Naasz for their leadership on the project, Kenneth Getzandanner for his expertise and help with the optical navigation, and Alex Pini and Marcelo Gonzales for providing the descent trajectory and their continued collaboration.

REFERENCES

[1] Mazanek, Daniel D., Merril, Raymond G., Brophy, John R., and Mueller, Robert P., "Asteroid Redirect Mission Concept: A Bold Approach For Utilizing Space Resources," Toronto, Canada, 2014.

[2] E. T. Lu and S. G. Love, "Gravitational tractor for towing asteroids," *Nature*, Vol. 438, Nov. 2005, pp. 177–178, 10.1038/438177a.

[3] D. M. Reeves, B. J. Naasz, C. A. Wright, and A. J. Pini, "Proximity Operations for the Robotic Boulder Capture Option for the Asteroid Redirect Mission," *AIAA SPACE 2014 Conference and Exposition*, American Institute of Aeronautics and Astronautics.

[4] D. Woffinden and L. Breger, "Automated Derivation and Verification of Navigation Requirements for On-orbit Rendezvous," *AIAA Guidance, Navigation, and Control (GNC) Conference*, Boston, MA, AIAA 2013-4964, 2013.

[5] P. S. Maybeck, *Stochastic Models, Estimation, and Control, Volume 1*. Orlando, FL: Academic Press, Inc., 1979.

[6] A. Gelb, *Applied Optimal Estimation*. Cambridge, MA: The M.I.T. Press, 1974.

[7] R. H. Battin, *An Introduction to the Mathematics and Methods of Astrodynamics*. 1801 Alexander Bell Drive, Reston, VA 20191: American Institute of Aeronautics and Astronautics, Inc., revised ed., 1999.

[8] D. K. Geller, "Linear Covariance Techniques for Orbital Rendezvous Analysis and Autonomous Onboard Mission Planning," *Journal of Guidance, Control, and Dynamics*, Vol. 29, November-December 2006, pp. 1404–1414.

[9] R. Zanetti, D. Woffinden, and A. Sievers, "Multiple Event Triggers in Linear Covariance Analysis for Spacecraft Rendezvous," *Journal of Guidance, Control, and Dynamics*, Vol. 35, March-April 2012, pp. 353–366.

[10] M. W. Busch, S. J. Ostro, L. A. Benner, M. Brozovic, J. D. Giorgini, J. S. Jao, D. J. Scheeres, C. Magri, M. C. Nolan, E. S. Howell, and others, "Radar observations and the shape of near-Earth Asteroid 2008 EV5," *Icarus*, Vol. 212, No. 2, 2011, pp. 649–660.

[11] "JPL Horizons," `http://ssd.jpl.nasa.gov/?horizons`. Accessed: 2014-12-19.

[12] J. R. Wertz, ed., *Spacecraft Attitude Determination and Control*. Dordrecht, Holland: D. Reidel Publishing Company, 1978.

[13] W. M. Owen Jr., "Methods of Optical Navigation," *21st AAS/AIAA Spaceflight Mechanics Meeting*, New Orleans, LA, 14 February 2011.

[14] Christopher D'Souza and Renato Zanetti, "The Optical Camera Measurement Model for Cislunar Navigation," Feb. 2014. FltDyn-CEV-14-XXX, MPCV Technical Brief.

[15] R. Gaskell, O. Barnouin-Jha, Daniel Scheeres, T. Mukai, N. Hirata, S. Abe, and J. Saito, "Landmark Navigation Studies and Target Characterization in the Hayabusa Encounter with Itokawa," Keystone, Colorado, American Institute of Aeronautics and Astronautics, Aug. 2006, AIAA 2006-6660.

[16] Joseph M. Galante, "Preliminary Analysis of GNFIR at NRL 2.0," Dec. 2012.

[17] Bong Wie, "Dynamics and Control of Gravity Tractor Spacecraft for Asteroid Deection," *Journal of Guidance, Control, and Dynamics*, Vol. 31, Oct. 2008, pp. 1413–1423.